Y. Hakmi, H. Miloudi, M. Miloudi, A. Gourbi, M.H. Bermaki

Frequency experimental identification approach for single-phase induction motor common-mode parameters

Introduction. *The presence of broad-spectrum and high-amplitude electromagnetic interference (EMI) within a single-phase induction motor (SPIM) drive poses a significant threat to both the system and other electronic equipment. High-frequency (HF) models of electrical motors play a critical role in overcoming these challenges, as they are essential for characterizing electromagnetic compatibility (EMC) in drives and designing effective EMI filters.* ***The novelty*** *of this study proposes an enhanced HF motor model based on transfer functions (TFs) to accurately represent the motor's behavior at HFs for frequency-domain analyses in the range of 100 Hz to 30 MHz.* ***Purpose.*** *The equivalent HF model for a SPIM is discussed in this paper. The suggested equivalent circuit describes a motor's common-mode (CM) properties.* ***Methodology.*** *HF model was developed by a frequency-domain analysis utilizing an experimental setup and MATLAB software. The motor impedance analysis is based on the measurement of variations in motor characteristics as a function of frequency in the CM setup.* ***Originality.*** *TF has been tuned using an asymptotic identification method of Bode to match the behavior of the real impedances of the motor parameters as a function of the frequency in the CM configuration. This tuned TFs are then synthesized into a comprehensive wideband EMC equivalent circuit model using the Foster network technique, which can be then simulated in any Spice-based simulator tools.* ***Results.*** *The proposed mathematical model was employed to conduct simulations, and the resulting predictions were validated against experimental data. CM response of the EMC equivalent circuit at low, medium, and HFs were compared between simulations and experimental measurements using Lt-Spice simulator software.* ***Practical value.*** *It is observed that results show satisfactory agreement with the measurements over a large frequency bandwidth [100 Hz–30 MHz], and the equivalent model of SPIM can be cascaded with other electronic and electrical modules to form a complete single-phase electric drive system model for fast analysis and prediction of system level EMI and electromagnetic sensitivity.* References 37, table 5, figures 13.
Key words: **common-mode, electromagnetic compatibility, experimental impedance measurement, high frequency, single-phase induction motor.**

Вступ*. Наявність широкоспектральних та високоамплітудних електромагнітних перешкод (ЕМП) в однофазному асинхронному електродвигуні (ОАЕД) становить значну загрозу як для системи, так і для іншого електронного обладнання. Високочастотні (ВЧ) моделі електродвигунів відіграють вирішальну роль у подоланні цих проблем, оскільки вони необхідні для характеристики електромагнітної сумісності (ЕМС) у приводах та проєктування ефективних фільтрів ЕМП.* ***Новизна*** *цього дослідження полягає в тому, що пропонується вдосконалена модель ВЧ-двигуна на основі передатних функцій (ПФ) для точного представлення поведінки двигуна на ВЧ для аналізу частотної області в діапазоні від 100 Гц до 30 МГц.* ***Мета****. У статті обговорюється еквівалентна ВЧ-модель для ОАЕД. Запропонована еквівалентна схема описує властивості двигуна у синфазному режимі (СР).* ***Методологія****. ВЧ-модель була розроблена за допомогою аналізу у частотній області з використанням експериментальної установки та програмного забезпечення MATLAB. Аналіз імпедансу двигуна заснований на вимірюванні змін характеристик двигуна в залежності від частоти встановлення СР.* ***Оригінальність****. ПФ були налаштовані за допомогою асимптотичного методу ідентифікації Боде для відповідності поведінці реальних імпедансів параметрів двигуна залежно від частоти конфігурації СР. Надалі ці налаштовані ПФ синтезуються в комплексну модель еквівалентної схеми ЕМС з використанням методу мережі Фостера, яку потім можна моделювати в будь-яких інструментах симулятора на основі Spice.* ***Результати****. Запропонована математична модель використовувалася щодо моделювання, а отримані прогнози було перевірено з урахуванням експериментальних даних. Реакція СР еквівалентної схеми ЕМС на низьких, середніх та високих частотах порівнювалась між моделюванням та експериментальними вимірами з використанням програмного забезпечення симулятора Lt-Spice.* ***Практична цінність****. Результати показують задовільне співпадіння з вимірюваннями у значному діапазоні частот [100 Гц-30 МГц], а еквівалентна модель ОАЕД може бути каскадована з іншими електронними та електричними модулями для формування повної моделі однофазної системи електроприводу для швидкого аналізу та прогнозування ЕМП на рівні системи та електромагнітної чутливості. Бібл. 37, табл. 5, рис. 13.*
Ключові слова: **синфазний режим, електромагнітна сумісність, експериментальний вимір імпедансу, висока частота, однофазний асинхронний двигун.**

Abbreviations

CM	Common-Mode	PSCM	Permanent Split Capacitor Motor
EMC	Electromagnetic Compatibility	PWM	Pulse Width Modulation
EMI	Electromagnetic Interference	SPIM	Single-Phase Induction Motor
FEM	Finite Element Method	TF	Transfer Function
HF	High-Frequency		

Introduction. Electric motors account for more than 53 % of electricity consumption in developed nations and approximately 65 % in the industrial sector [1]. SPIMs boast efficiencies ranging from 30 % to 65 %, rendering them popular for low power applications [2]. SPIM drivers find applications in a wide range of equipment, including domestic and industrial settings, for controlling pumping operations [3], variable speed fans [4], compressors [5] and vehicle electric systems [6].

Using a variable frequency driver with SPIM (Fig. 1) offers numerous advantages in terms of speed control, energy efficiency, starting torque, noise and vibration [4]. This combination is finding increasing use in a wide range of applications [3–6].

Researchers are investigating diverse driving technologies to improve the performance and efficiency of SPIMs, prompted by concerns regarding operational costs and energy consumption [7, 8]. Adapting SPIM speed to loading conditions optimizes energy savings and system performance through PWM inverter control (Fig. 1). However, internal HF switching in PWM inverters induces significant voltage changes (d*v*/d*t*), causing serious CM EMI issues. These challenges have a substantial impact on the EMC of the system. SPIMs play a central role in amplifying these disturbances as they serve as the primary conduit for the propagation of CM currents.
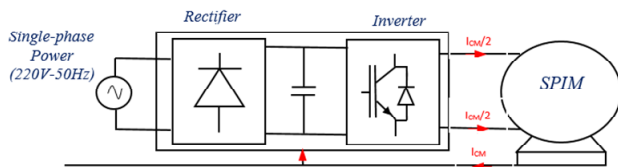
Fig. 1. Topology of SPIM driven by the single-phase inverter

Furthermore, the presence of CM voltage in the motor's output can give rise to various issues, including leakage current, shaft voltage, and bearing currents. These complications not only substantially reduce the life cycle of machines and drives but also have the potential to violate international EMI standards [9–12]. Therefore, responsible management of these technologies is crucial to both maximize the benefits and mitigate the risks associated with EMI.

Given the complexity of power generation and transmission in electric drive systems, conventional post processing methods relying on experience and experimentation are insufficient for precisely identifying and addressing EMC issues [13–15]. Therefore, establishing advanced system level EMI simulation, prediction, and optimization design methods is imperative during the early stages of SPIM driver development.

In this context, assessing CM impedance characteristics at HFs for the SPIM is crucial. The CM impedance of SPIMs significantly influences the magnitude of CM currents induced by the CM voltage of the inverter in SPIM drive systems. SPIMs contribute to CM currents due to their intrinsic asymmetry and the presence of parasitic capacitance and inductance inherent in their design. At HFs, these parasitic elements become more pronounced and can substantially affect the CM impedance of the motor. The impedance of these parasitic elements varies with frequency, resulting in complex networks and changes in the overall CM impedance of the motor. Understanding CM impedance up to 30 MHz is essential to ensure compliance with stringent EMC standards established by organizations like the International Special Committee on Radio Interference [16], which govern conducted EMI assessments across frequencies ranging from 150 kHz to 30 MHz.

Previous research on SPIMs has primarily concentrated on design optimization [8, 17], fault diagnosis [18, 19], and control methodologies [2, 4–7, 20], resulting in notable enhancements in SPIM performance and operational efficiency. However, there exists a notable gap in understanding the electromagnetic behavior of SPIMs from an EMC perspective. While some studies have explored EMC aspects, such as the work of [9], which focused on EMC characterization of capacitor start SPIMs using a HF model based on a genetic algorithm, further research is needed to address this gap. **This paper aims** to address this gap by introducing a pioneering study on the electromagnetic behavior of SPIMs with start capacitors from an EMC perspective. Through the development of a comprehensive HF model tailored specifically for start capacitor SPIMs based on motor port impedance characteristics, the objective is to investigate their electromagnetic characteristics, including CM impedance and propagation paths. By incorporating advanced simulation and predictive modeling techniques, this model enhances the electromagnetic environment of adjustable drive systems, enabling accurate investigation

and proactive resolution of EMI issues. Specifically, the model effectively addresses critical EMI concerns such as motor terminal overvoltage ringing and bearing discharge current, facilitating the design of effective dv/dt filters and improving overall EMC performance.

HF SPIM model. Researchers have proposed diverse EMI modeling approaches for various electrical machines, including three phase induction motors [21–28], DC motors [11, 29], and permanent magnet machines [12, 30–32]. These approaches fall into two main categories: FEM and measurement-based methods, a numerical technique, adeptly capture the intricate geometry and material characteristics of machines. Employed in the preliminary design phase, engineers use FEM to assess the impact of motor design choices on undesirable HF phenomena, establishing a 3D or 2D electromagnetic analysis that requires an understanding of the motor's geometric structure and electromagnetic parameters [12, 30, 31]. However, this method not only increases the workload for researchers, but also places limitations on the model's accuracy at higher frequencies.

In contrast, measurement-based methods rely on experimental data from impedance measurements, usually in common and differential modes, and involve a parameterization process. They provide higher accuracy than numerical models, do not require detailed motor geometry, and are well-suited for system level simulations predicting HF phenomena such as overvoltage and conducted emissions. The main types of measurement-based models are the physics-based circuits, and the behavioral or black-box models. Physics-based circuits use pre-defined equivalent circuit topologies with parameters that reflect the physical components of the machine to represent the real HF behavior of the machine. Some examples of physics-based circuit models can be found in [22, 23, 26, 29]. Although they have a rather low number of circuit elements and therefore low complexity, they need an extraction procedure to determine the unknown circuit parameters, and most of them are only validated up to 10 MHz. Black-box models adeptly represent dynamic behaviors, especially in HF resonances, accounting for complex internal structures and parasitic coupling in electrical machines. Rational functions achieve this by easily converting to equivalent electric circuits, accurately reproducing measured behaviors at terminals [14, 25, 27, 28, 33].

In [20] was presented a broadband equivalent circuit model for three phase AC motors using the vector fitting algorithm. Despite its high accuracy in capturing resonance behavior across a broad frequency range, the method's complexity in mathematical procedures may constrain its practical application.

In summary, previous relevant studies in EMC and HF electrical machine modeling have identified several limitations. These include:

1. A notable gap in HF modeling, particularly tailored for SPIM, despite facing analogous challenges to three phase motors.

2. The precision of existing modeling approaches relies heavily on the detailed internal structural features of the machine.

3. The proposed modeling methods face challenges in meeting EMI requirements, primarily because of constraints in effectively handling the required frequency ranges (150 kHz – 30 MHz).

Addressing the aforementioned issues, this paper proposes a measurement-based wide-frequency EMC model for the PSCM, treating the motor as a black box. The model accurately depicts CM characteristics from 100 Hz to 30 MHz, offering key analyses of EMI emission and coupling mechanisms in a single-phase electric drive system. A 175 W SPIM with PSCM is utilized as a case study. The CM port impedance, is mathematically fitted using Bode's asymptotic identification method. The resulting tuned TF is synthesized into an EMC equivalent circuit using the RLC Foster network.We validate the model's effectiveness and accuracy by comparing it with experimental results using the Lt-Spice simulator. Besides modeling the behavior of the PSCM, this article explores the influence of internal parameters on the EMC behavior of the motor. Crucially, it identifies dominant effects at specific frequencies. The analysis encompasses CM of dominant parasitic capacitances within the electric machine critical for understanding primary motor-to-ground CM pathways.

Key properties of the proposed model:

1. The model identification process is straightforward, achieving high accuracy by relying only on the impedance magnitude and phase angle of the structure's parasitic parameters, independent of motor manufacturer data.

2. The equivalent circuit model seamlessly integrates with other components to form complete electric drive system models, enabling thorough assessment of conducted emissions and ensuring EMC compliance. It accurately predicts stator winding overvoltage and bearing discharge current, facilitating optimal design of mitigation measures such as dv/dt filters.

3. The methodology is versatile and can be extended to each individual component in the drive system (e.g., cable, inverter), allowing its application across a wide range of motors.

The proposed method provides the capability to characterize the motor impedance over a wide frequency range, which is one of its key practical advantages. This enables designers to more effectively adjust the motor parameters to ensure optimal performance under varying operating conditions, a crucial necessity for many industrial and commercial applications such as pumping or ventilation. Given that variable speed drives operate at HF, it becomes imperative to find a HF model of the motor associated with the variable speed drive. This method thus allows for modeling the motor behavior under extreme conditions.

CM measurement setup for PSCM. SPIM, resembling the design of a three-phase motor, consists of a stator and a squirrel-cage rotor with two perpendicular windings: primary «running» and auxiliary «starting». Upon motor initiation, a centrifugal switch disconnects the auxiliary winding at around 75 % of the nominal speed [8, 20]. PSCM is a specialized variant known for its incorporation of a start split capacitor [2]. In this configuration, the auxiliary winding, and capacitor are connected in series, enhancing the motor's starting efficiency. The capacitor plays a crucial role in optimizing the initial startup process. Specific motor characteristics examined in this paper are detailed in Table 1.

The Wayne Kerr 6500B precision impedance analyzer for impedance analysis are used. This analyzer offers high resolution measurements from 100 Hz to 30 MHz, meeting the IEEE Std 112-2017 reliability requirements. With an impressive impedance accuracy of ±0.05 %.

Table 1
PSCM parameters

Rated voltage, V	Rated power, W	Rated current, A	Speed, rpm	Rated torque, N·m	Efficiency, %
230	<175	<1.5	1400	<4	87

To anticipate HF behavior, the impedance between the motor terminals and the housing was assessed using the configuration shown in Fig. 2. This approach provided insights into the CM characteristics of the tested PSCM.
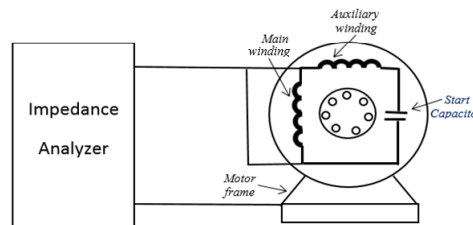

Fig. 2. CM test configuration

Figures 3, 4 show that this impedance starts to be capacitive due to the parasitic capacitance between the stator windings and the motor frame. Then, at medium frequency, the parasitic inductance becomes more dominant, so that the CM impedance drops at a certain frequency, and multiple peaks and drops can occur thereafter. However, at HFs, beyond the antiresonance frequency f_n, Z_{CM} demonstrates a weaker increase and exhibits inductive behavior.
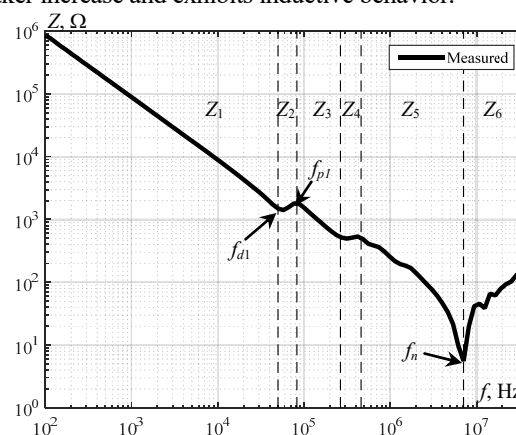

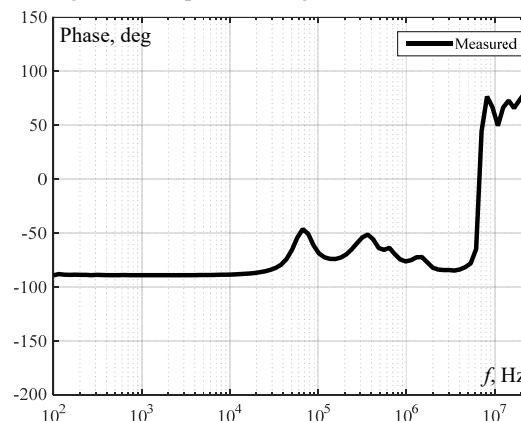Fig. 3. CM impedance magnitude measurement

Fig. 4. CM impedance phase measurement

HF modeling of the CM impedance of the PSCM. The obtained measurement results facilitate the progression to the subsequent stage, where the TF is modeled. Specifically, Bode's asymptotic identification method is applied to model the magnitude and phase of the CM

impedance. The approach involves extracting the impedance TF for PSCM, utilizing the identification method. The modeling strategy is grounded in the observation that the overall magnitude curve of the impedance measurement undergoes a change in slope at each break frequency. Additional details about the method can be found in [34–36].

The modeling process involves the following succinct steps:

1. Identify break frequencies (pole and zero positions) from measured data, as depicted in Fig. 3.

2. Define the slopes of asymptotes and terms for the corresponding TF segments.

3. Derive the comprehensive system TF by multiplying the TFs at different frequencies.

From the characteristics of the magnitude depicted in Fig. 3, several break frequencies f_{d1}, f_{p2},..., f_n related to the poles and zero's locations have been exhibited. The asymptotic magnitude Bode plots of basic TFs terms are used to obtain the approximate plot for the real CM impedance.

Before the first dipping frequency f_{d1}, the magnitude curve decreases with a slope of -1, and the phase is $-90°$:

$$Z_1(s) = 1 / s, \qquad (1)$$

where s is the Laplace transform variable or complex frequency; $Z_1(s)$ is the TF of the pole at the origin.

At the first dipping and peaking frequencies (f_{d1} and f_{p2}) suggest the presence of 2nd-order systems (ξ_2 and ξ_3 are the damping ratios). The corresponding terms are calculated by:

$$Z_2(s) = \left[\left(\frac{1}{w_{n2}^2}\right) \cdot s^2 + \frac{2 \cdot \xi_2}{w_{n2}} \cdot s + 1\right], \qquad (2)$$

where $Z_2(s)$ is the TF of a 2nd-order system; the undamped natural frequency w_{n2} is given by:

$$w_{n2} = 2 \cdot \pi \cdot f_{d1}, \qquad (3)$$

$Z_3(s)$ is for 2nd-order system with two poles:

$$Z_3(s) = \frac{1}{\left[\left(\frac{1}{w_{n3}^2}\right) \cdot s^2 + \frac{2 \cdot \xi_3}{w_{n3}} \cdot s + 1\right]}, \qquad (4)$$

where the undamped natural frequency w_{n3} is given by:

$$w_{n3} = 2 \cdot \pi \cdot f_{p2}. \qquad (5)$$

Applying the same analysis to each pair of remaining dipping and peaking frequencies in the CM impedance measurement yields TFs at different frequencies. The complete TF is obtained by:

$$Z_{CM}(s) = Z_1(s) \cdot Z_2(s) \cdots Z_n(s). \qquad (6)$$

The estimated CM TF can be expressed as a ratio of two frequency-dependent polynomial representations:

$$Z_{CM}(s) = \frac{b_m \cdot s^m + b_{m-1} \cdot s^{m-1} + \cdots + b_1 \cdot s + b_0}{a_n \cdot s^n + a_{n-1} \cdot s^{n-1} + \cdots + a_1 \cdot s + a_0}, \qquad (7)$$

where a_n, $b_m \in$ Re are the unknown polynomial coefficients; n is the order of the desired model.

The coefficients of the Z_{CM} TF are given in Table 2.

Figures 5, 6 display the frequency response of the estimated TF compared to the measurement curves. This comparison reveals the superposition of curves for both the magnitude and phase of the CM impedance from 100 Hz to 30 MHz, sufficiently confirming the validity of the modeling principle in the CM frequency range. To achieve a better approximation, introducing more poles and zeros into the TF is advisable. However, our primary aim is to obtain a less complex yet more physically accurate model.
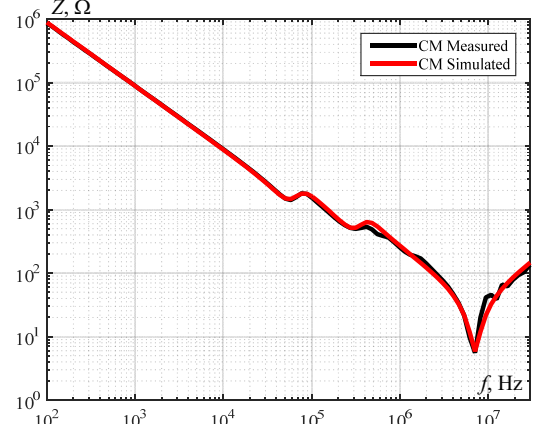

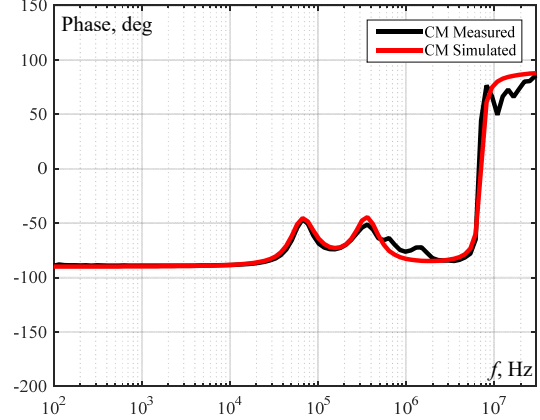Fig. 5. Measured and simulated magnitudes of CM impedance

Fig. 6. Measured and simulated phases angle of CM impedance

Figure 7 shows the pole-zero distribution in the complex frequency plane. As we can see, all the poles of the polynomial function are located on the left half-plane, which gives us sufficient information about the stability of the system.
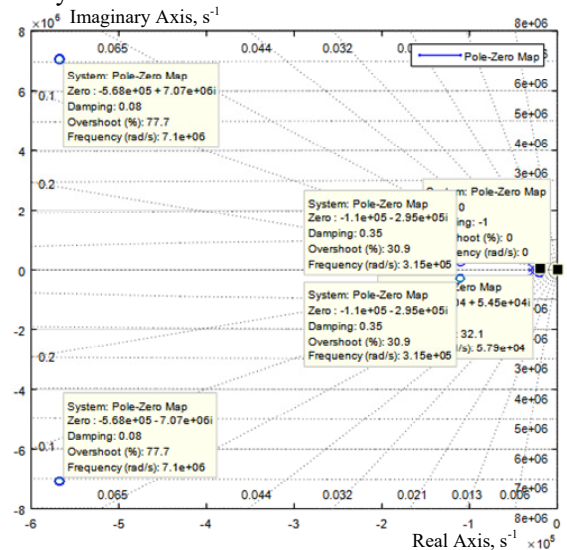

Fig. 7. Zero and pole locations of the CM impedance

Table 2

Coefficients of the 5th-order TF

a_0	a_1	a_2	a_3	a_4	a_5
0	$9.322 \cdot 10^{20}$	$1.088 \cdot 10^{16}$	$1.844 \cdot 10^{11}$	$3.692 \cdot 10^5$	1

b_0	b_1	b_2	b_3	b_4	b_5	b_6
$8.245 \cdot 10^{28}$	$1.152 \cdot 10^{24}$	$2.756 \cdot 10^{19}$	$6.49 \cdot 10^{13}$	$2.491 \cdot 10^8$	6.849	$4.908 \cdot 10^6$

Approach to get PSCM equivalent circuit. This section delves into the practical approach for the successful passive network synthesis of the TF of PSCM, utilizing the approximate Foster equivalent method. The goal is to propose a Spice-compatible equivalent circuit that accurately reproduces the frequency response of the CM impedance. To achieve this, a series of steps must be undertaken, starting with the expansion of the previously derived TF into a partial fraction representation, specifically pole-residue pairs. Subsequently, this representation is synthesized into a series of parallel combinations of resistance, inductance, and capacitance, as illustrated in Fig. 8, at which the subscripts *r* and *c* indicate the real and complex numbers and their orders are *Nr* and *Nc* for real and pair complex poles respectively.
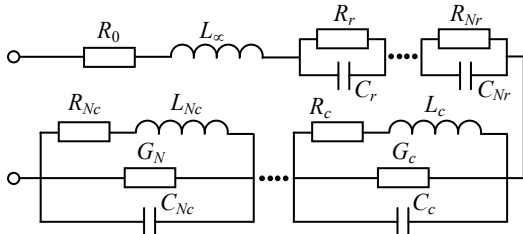

Fig. 8. Equivalent circuit synthesis for the Foster expansion of TF

Pole-residue formulation. The process of obtaining the partial fraction expansion of the CM TF (7) simply involves reexpressing the ratio of the polynomial representation into a sum of simpler positive real functions $Z_1(s)$, $Z_2(s),\ldots, Z_n(s)$, as follows:

$$Z_{CM}(s) = \frac{\sum_{m=0}^{M} b_m \cdot s^m}{\sum_{n=0}^{N} a_n \cdot s^n} = d + e \cdot s + \sum_{n=1}^{N_r} \frac{r_{rn}}{s - p_{rn}} +$$

$$+ \sum_{n=1}^{N_c}\left(\frac{r_{cn}}{s - p_{cn}} + \frac{r_{cn}^*}{s - p_{cn}^*} \right);$$

(8)

where d is the real value constant; e is the s-proportional term; N_r, N_c are the numbers of real poles and complex conjugate pole pairs; p_{rn}, r_{rn} are the real poles and residues; p_{cn}, p_{cn}^*, r_{cn}, r_{cn}^* are the pairs of complex and conjugate poles and residues respectively.

Equivalent circuit synthesis. Converting the partial fraction expansion (8) into an equivalent circuit compatible with Spice [37]. Table 3 summarizes the synthesis methods for real-pole and complex-pole pair terms.

Table 3

The equivalent circuit synthesis of Z_{CM} TF

$Z(s)$	Equivalent circuit model	Parameters
$d + e \cdot s$		$R_0 = d;\quad L_\infty = e$
$r_r / (s - p_r)$		$R_r = -r_r / p_r;\quad C_r = 1/r_r$
$\dfrac{r_c}{s - p_c} + \dfrac{r_c^*}{s - p_c^*}$		$R_c = \dfrac{L_c(r_c p_c^* + r_c^* p_c)}{r_c + r_c^*}$
		$L_c = \dfrac{r_c + r_c^*}{p_c p_c^* + \left[-(p_c^* + p_c) + \dfrac{r_c p_c^* + r_c^* p_c}{r_c + r_c^*} \right] \dfrac{r_c p_c^* + r_c^* p_c}{r_c + r_c^*}}$
		$G_c = \dfrac{r_c + r_c^*}{-(p_c^* + p_c) + \dfrac{r_c p_c^* + r_c^* p_c}{r_c + r_c^*}}$
		$C_c = 1/\left(r_c + r_c^* \right)$

A calculation was conducted to determine the values of the circuit components. The extracted poles and residues are presented in Table 4, while the synthesized component values for the equivalent circuit HF model of the PSCM – in Table 5.

Table 4

Poles and residues of the TF of Z_{CM}

$d = 5.03626;\quad e = 4.90827 \cdot 10^{-6}$	
Poles p_i	Residues r_i
$p_r = 0$	$r_r = 5.5573 \cdot 10^8$
$p_c = -1.769 \cdot 10^5 \pm i \cdot 4.442 \cdot 10^5$	$r_c = 1.957\text{e}8 \pm i \cdot 3.537 \cdot 10^7$
$p_c = -9.831 \cdot 10^5 \pm i \cdot 2.321 \cdot 10^6$	$r_c = 3.002\text{e}8 \pm i \cdot 8.108 \cdot 10^7$

The frequency responses obtained from measurements and the equivalent circuit using the Lt-Spice simulator are compared in Fig. 9, 10.

Table 5

Component values of the equivalent circuit

$R_0 = 5.0362\ \Omega$		$L_\infty = 7.8117 \cdot 10^{-7}$ H		
Real branch no.		R_r, Ω		C_r, F
1		0		$1.7994 \cdot 10^{-9}$
Branch no.	L_c, H	R_c, Ω	C_c, F	G_c, S
1	$1.04 \cdot 10^{-4}$	37.01	$1.66 \cdot 10^{-9}$	3730
2	$1.92 \cdot 10^{-3}$	185.7	$2.55 \cdot 10^{-9}$	1522.4

As depicted in Fig. 9 and detailed in Table 5, the variation in CM impedance for PSCM with frequency is effectively represented by a series connection of the components: resistance R_0, inductance L_∞ and capacitance C_r. This model is particularly relevant in the frequency range of 100 Hz to 7 MHz, where C_r signifies the capacitive interaction between the stator windings and the

motor frame. Above 7 MHz, the predominantly inductive behavior is attributed to the inductance L_∞, wherein the main impact is observed in the internal and external feed lines of the motor. Simultaneously, resistance R_0 plays a crucial role in damping the resonance that results from the interaction between L_∞ and C_r. Two additional R-L-C-G branches are introduced, cascading with the previous components to capture further resonant phenomena. The first cell resonates at 80 kHz, while the second cell represents the resonance frequency at 446 kHz.
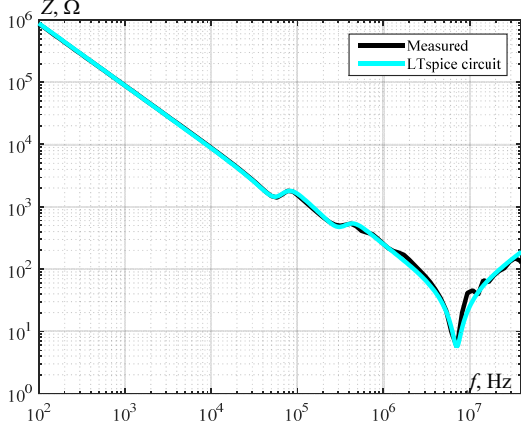

Fig. 9. Comparison of measurement and simulated magnitude of a Foster equivalent circuit for CM impedance
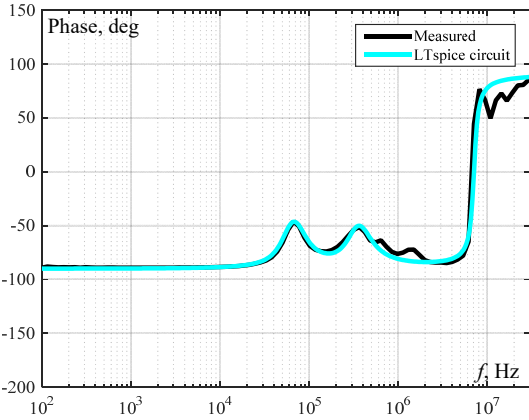

Fig. 10. Comparison of measurement and simulated phase of a Foster equivalent circuit for CM impedance

CM impedance analysis in PSCM based on motor parameters. Graphing impedance characteristics of the main winding Z_m, auxiliary winding Z_a and start capacitor Z_c in a CM up to 30 MHz offers insights into the frequency-dependent behavior of the SPIM. In Fig. 11 the measurement configurations for motor parameters are described, and the impedance frequency responses are presented in Fig. 12, 13. The measurement setup involves connecting the two probes of the precision impedance analyzer between the terminals of each parameter shorted together and the motor frame.

Initial impedance comparison observations reveal a decline in spectrum amplitudes with slopes of (–1) at low frequencies. The impedances of the CM Z_{CM}, main Z_m and auxiliary Z_a windings overlap, indicating capacitive behavior attributed primarily to parasitic capacitances between conductors and slot walls. Their impact is minimal at 100 Hz due to typically large impedance. However, as frequency increases, impedance decreases, promoting the circulation of CM current.
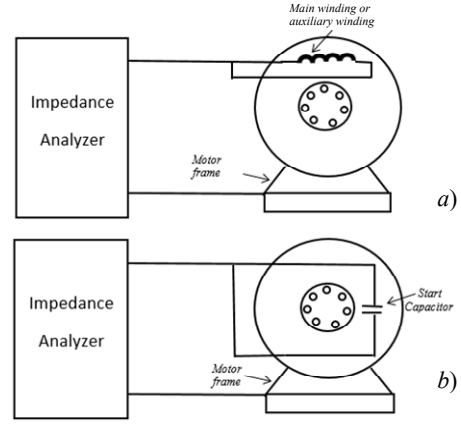

Fig. 11. Measurement setups of the main or auxiliary winding (*a*) and start capacitor (*b*)
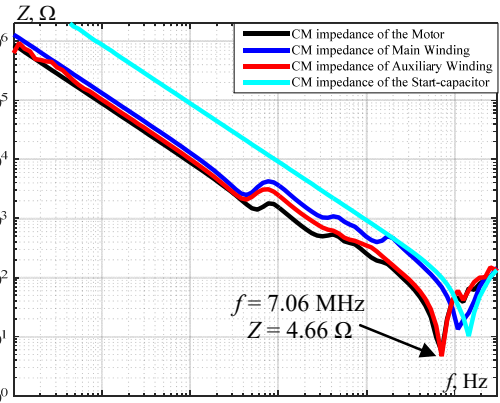

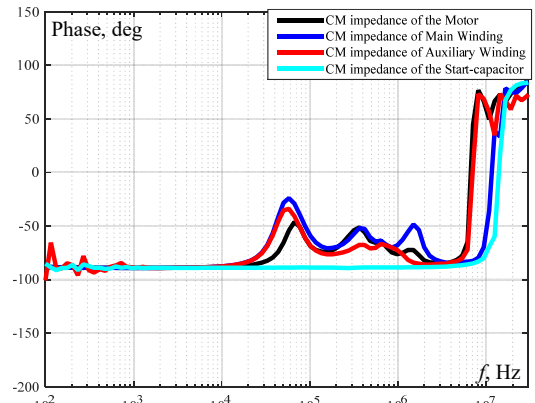Fig. 12. Magnitude evolution of the PSCM parameters

Fig. 13. Phase angle evolution of the PSCM parameters

In the medium-frequency range, interactions among inductive, resistive, and capacitive elements govern motor impedances, exhibiting multiple resonances and anti-resonances in the impedance modulus. This spectrum distribution highlights electromagnetic diversity within the motor. Results show a parallel trend in the number and shape of resonances between the CM impedance of PSCM and the main impedance, indicating the significant influence of dominant parasitic capacitances from the main winding. This profoundly impacts PSCM's CM impedance behavior, with parasitic capacitances in the main winding becoming the primary path for CM currents at specific frequencies.

At higher frequencies, impedances continue to decrease with slopes of (–1), signifying reduced impedance of parasitic capacitances and decreased CM current resistance. Results emphasize the significant impact of the auxiliary

winding on shaping the motor's CM impedance characteristics within this frequency range. This underscores the substantial influence of the auxiliary winding on the CM impedance of PSCM, with associated parasitic capacitances creating a low impedance route and establishing new current flow paths within the motor. Notably, at the antiresonance frequency of 7 MHz, the motor impedance is only 4.66 Ω, representing the lowest impedance path for CM leakage current across the frequency range. At this frequency, CM current through the auxiliary winding can be significant, posing a risk of stator winding failure. Therefore, careful consideration in EMC design is required to assess the current driven by the CM voltage of the voltage source inverter. Additionally, the start capacitor has no significant effect on total CM impedance, allowing its influence on the HF model to be neglected.

Understanding these paths is vital for assessing risks linked to CM current. CM noise circulation, driven by dominant parasitic capacitances at specific frequencies, poses threats to motor efficiency and interconnected equipment performance. Increased motor heating from CM current may lead to premature aging, while interference with control circuits can cause erratic behavior and reduced system reliability. To mitigate risks, consider strategies like filters, optimized grounding, and shielding.

This study examined the implications of modeling results for practical applications, such as environmental impact, potential effects of SPIM, and the mode of circulation of common currents in SPIMs. The models could be used to improve the electromagnetic environment of adjustable drive systems, thus ensuring optimal operation while avoiding EMC compatibility issues. Furthermore, these results could be used to develop a model for an adjustable drive system. On the other hand, by considering the model of the motor implanted in a variable speed drive system, researchers could identify conducted emissions generated by this system. Through simulation, engineers can quantify EMI noise amplitude and propagation paths within the system, including overvoltage amplitude and waveform. This requires developing an accurate HF model of key motor driving components, SPIM, cables, and inverters. Consequently, EMI reduction techniques can then be proposed based on such HF EMI models, minimizing interference risks and enhancing EMC of the system.

Conclusions. This paper introduces a practical method to model the common-mode impedance of permanent split capacitor motor across a wide range of frequencies relevant to conductive common-mode electromagnetic interference. Common-mode impedance for single-phase induction motor with 175 W has been measured, tested and utilized to synthesize the motor equivalent circuit. The simulated data closely aligns with the experimental data up to 30 MHz. The accuracy relies on the order of approximation. Moreover, the impact of each parameter of the permanent split capacitor motor on the common-mode impedance has been investigated in a wide frequency range. Results indicate that the auxiliary winding notably influences the main path of the high-frequency common-mode current, as this is the key for the electromagnetic compatibility optimization. The model is presented as Spice circuits, allowing for direct inclusion into a circuit model suitable for predicting terminal overvoltage and addressing electromagnetic interference issues.

Additionally, it can predict and address high-frequency problems and aid in designing electromagnetic interference filters to enhance electromagnetic compatibility in cable-fed motor-drive systems.

Conflict of interest. The authors of the article declare that there is no conflict of interest.

REFERENCES

1. Gómez J.R., Quispe E.C., Castrillón R. del P., Viego P.R. Identification of Technoeconomic Opportunities with the Use of Premium Efficiency Motors as Alternative for Developing Countries. *Energies*, 2020, vol. 13, no. 20, art. no. 5411. doi: https://doi.org/10.3390/en13205411.
2. Jannati M., Anbaran S.A., Asgari S.H., Goh W.Y., Monadi A., Aziz M.J.A., Idris N.R.N. A review on Variable Speed Control techniques for efficient control of Single-Phase Induction Motors: Evolution, classification, comparison. *Renewable and Sustainable Energy Reviews*, 2017, vol. 75, pp. 1306-1319. doi: https://doi.org/10.1016/j.rser.2016.11.115.
3. Bojang D., Nhantumbo E., Verma M., Kulkarni A. PV-Fed Single-Phase Induction Motor for Irrigation Application. *Journal of The Institution of Engineers (India): Series B*, 2024, vol. 105, no. 2, pp. 335-342. doi: https://doi.org/10.1007/s40031-023-00975-z.
4. Kiriella K.K.C.S., Karunadasa J.P., Rodrigo W.D.A.S. Design and Implementation of an Electronic Fan Regulator for Reduced Harmonics and Ripple Free Speed. *Engineer: Journal of the Institution of Engineers*, Sri Lanka, 2023, vol. 56, no. 4, pp. 13-22. doi: https://doi.org/10.4038/engineer.v56i4.7588.
5. Önceler A.A., Taşkin S. Modeling and analysis of single-phase induction motor drive for variable capacity control of a refrigerator compressor. *Sigma Journal of Engineering and Natural Sciences*, 2020, vol. 38, no. 3, pp. 1509-1526.
6. Rusdi M., Jayadi J., Mangera P., Ponadi A., Wakole P. Speed Control of Induction Motor Using Variable Frequency Driver (VFD) Method Based On Arduino Nano. *MATEC Web of Conferences*, 2022, vol. 372, art. no. 06001. doi: https://doi.org/10.1051/matecconf/202237206001.
7. Phurahong T. Design of 2-Leg Inverter for Controlling of A Single Phase Induction Motor. *2020 3rd International Conference on Power and Energy Applications (ICPEA)*, 2020, pp. 117-120. doi: https://doi.org/10.1109/ICPEA49807.2020.9280147.
8. Rahman S., Meraj M., Iqbal A., Tariq M., Maswood A.I., Ben-Brahim L., Al-ammari R. Design and Implementation of Cascaded Multilevel qZSI Powered Single-Phase Induction Motor for Isolated Grid Water Pump Application. *IEEE Transactions on Industry Applications*, 2020, vol. 56, no. 2, pp. 1907-1917. doi: https://doi.org/10.1109/TIA.2019.2959734.
9. Miloudi H., Miloudi M., Ardjoun S.A.E.M., Mahmoud M.M., Telba A.A., Denaï M., Khaled U., Ewais A.M. Electromagnetic Compatibility Characterization of Start-Capacitor Single-Phase Induction Motor. *IEEE Access*, 2024, vol. 12, pp. 2313-2326. doi: https://doi.org/10.1109/ACCESS.2023.3349018.
10. Zeghoudi A., Slimani H., Bendaoud A., Benazza B., Bechekir S., Miloudi H. Measurement and analysis of common and differential modes conducted emissions generated by an AC/DC converter. *Electrical Engineering & Electromechanics*, 2022, no. 4, pp. 63-67. doi: https://doi.org/10.20998/2074-272X.2022.4.09.
11. Bermaki D.M.H., Miloudi D.H., Miloudi D.M., Gourbi D.A., Bendaoud P.D.A. High-frequency Differential Mode Modeling of Universal Motor's Windings. *International Journal of Electrical and Electronics Research*, 2023, vol. 11, no. 4, pp. 1057-1064. doi: https://doi.org/10.37391/ijeer.110425.
12. Ruiz-Sarrio J.E., Chauvicourt F., Gyselinck J., Martis C. Impedance Modeling Oriented Toward the Early Prediction of High-Frequency Response for Permanent Magnet Synchronous Machines. *IEEE Transactions on Industrial Electronics*, 2023, vol. 70, no. 5, pp. 4548-4557. doi: https://doi.org/10.1109/TIE.2022.3189075.
13. Zheng F., Wang A., Wu Z., Gao T., Wang Z., Zhao X. Capacitor Tolerance Criterion for Three-Phase EMI Filters to Attenuate Noise of PWM Inverters. *IEEE Transactions on Power Electronics*, 2021, vol. 36, no. 8, pp. 9080-9092. doi: https://doi.org/10.1109/TPEL.2020.3048272.
14. Xiong Y., Li X., Zhou W., Li N., Jiao M., Li Y., Du X., Nie X., Ji X. Broadband Electromagnetic Compatibility Modeling for Three-Phase

Synchronous Motor of Armored Vehicle. *Acta Armamentarii*, 2022, vol. 43, no. 7. pp. 1467-1477. doi: https://doi.org/10.12382/bgxb.2021.0387.
15. Han D., Li S., Wu Y., Choi W., Sarlioglu B. Comparative Analysis on Conducted CM EMI Emission of Motor Drives: WBG Versus Si Devices. *IEEE Transactions on Industrial Electronics*, 2017, vol. 64, no. 10, pp. 8353-8363. doi: https://doi.org/10.1109/TIE.2017.2681968.
16. CISPR 22. *Information technology equipment – Radio disturbance characteristics – Limits and methods of measurement*. Edtion 6.0, August 2008.
17. Sharma U., Singh B. Improved Design for High Efficiency of Single-Phase Induction Motor for Industrial Exhaust Fan. *2021 IEEE 4th International Conference on Computing, Power and Communication Technologies (GUCON)*, 2021, pp. 1-5. doi: https://doi.org/10.1109/GUCON50781.2021.9573780.
18. Ganguly B., Chatterjee A., Chatterjee A., Paul S. Diagnosis of Stator Winding Fault of Single-Phase Induction Motor Employing Wavelet Induced Residual-Convolutional Neural Network. *2020 IEEE International Conference on Power Electronics, Drives and Energy Systems (PEDES)*, 2020, pp. 1-5. doi: https://doi.org/10.1109/PEDES49360.2020.9379665.
19. Alviento E.V., Cabais J.B., Fajardo J.M.M., Garcia R.G., Ballado A.H. Early Detection of Single-Phase Induction Motor Failure through the use of Accelerometer and Temperature Sensor via Arduino. *2021 IEEE 17th International Colloquium on Signal Processing & Its Applications (CSPA)*, 2021, pp. 64-69. doi: https://doi.org/10.1109/CSPA52141.2021.9377285.
20. Golsorkhi M.S., Binandeh H., Savaghebi M. Online Efficiency Optimization and Speed Sensorless Control of Single-Phase Induction Motors. *Applied Sciences*, 2021, vol. 11, no. 19, art. no. 8863. doi: https://doi.org/10.3390/app11198863.
21. Miloudi H., Miloudi M., Gourbi A., Bermaki M.H., Bendaoud A., Zeghoudi A. A high-frequency modeling of AC motor in a frequency range from 40 Hz to 110 MHz. *Electrical Engineering & Electromechanics*, 2022, no. 6, pp. 3-7. doi: https://doi.org/10.20998/2074-272X.2022.6.01.
22. Zhao Z., Fan F., Sun Q., Jie H., Shu Z., Wang W., See K.Y. Physics Informed Neural Network-based High-frequency Modeling of Induction Motors. *Chinese Journal of Electrical Engineering*, 2022, vol. 8, no. 4, pp. 30-38. doi: https://doi.org/10.23919/CJEE.2022.000036.
23. Zhao Z., Fan F., Sun Q., Tu P., See K.Y. High-Frequency Modeling of Induction Motor Using Multilayer Perceptron. *2022 Asia-Pacific International Symposium on Electromagnetic Compatibility (APEMC)*, 2022, pp. 222-224. doi: https://doi.org/10.1109/APEMC53576.2022.9888414.
24. Karakasli V., Ye Q., Griepentrog G., Wei J. A Parameterization of 6-Port High-Frequency Delta- and Star-Connected Induction Motor Model. *2020 International Symposium on Electromagnetic Compatibility - EMC EUROPE*, 2020, pp. 1-6. doi: https://doi.org/10.1109/EMCEUROPE48519.2020.9245646.
25. Li L., He W., Wang Y., Li X. Modelling of the wide frequency equivalent circuit of the three-phase AC motor based on vector fitting method. *International Journal of Electric and Hybrid Vehicles*, 2019, vol. 11, no. 1, pp. 12-22. doi: https://doi.org/10.1504/IJEHV.2019.098722.
26. Toulabi M.S., Wang L., Bieber L., Filizadeh S., Jatskevich J. A Universal High-Frequency Induction Machine Model and Characterization Method for Arbitrary Stator Winding Connections. *IEEE Transactions on Energy Conversion*, 2019, vol. 34, no. 3, pp. 1164-1177. doi: https://doi.org/10.1109/TEC.2019.2891349.

27. Jia K., Bohlin G., Enohnyaket M., Thottappillil R. Modelling an AC motor with high accuracy in a wide frequency range. *IET Electric Power Applications*, 2013, vol. 7, no. 2, pp. 116-122. doi: https://doi.org/10.1049/iet-epa.2012.0127.
28. Idir N., Weens Y., Moreau M., Franchaud J.J. High-Frequency Behavior Models of AC Motors. *IEEE Transactions on Magnetics*, 2009, vol. 45, no. 1, pp. 133-138. doi: https://doi.org/10.1109/TMAG.2008.2006006.
29. Liu J., Wang X., Nan J. Application of Ant Colony Algorithm to the Analysis of Common Mode EMI Model of DC Motor. *Energy and Power Engineering*, 2011, vol. 3, no. 2, pp. 96-106. doi: https://doi.org/10.4236/epe.2011.32013.
30. Ruiz-Sarrio J.E., Chauvicourt F., Gyselinck J., Martis C. High-Frequency Modelling of Electrical Machine Windings Using Numerical Methods. *2021 IEEE International Electric Machines & Drives Conference (IEMDC)*, 2021, pp. 1-7. doi: https://doi.org/10.1109/IEMDC47953.2021.9449561.
31. Rahimi A., Kanzi K. Improved High-Frequency Modeling of PMSM Using 3-D Finite Element Analysis. *2019 International Power System Conference (PSC)*, 2019, pp. 71-78. doi: https://doi.org/10.1109/PSC49016.2019.9081510.
32. Zhang D., Kong L., Wen X. A measurement based modeling method of interior permanent magnet motor considering the rotor position for EMI analysis. *2014 IEEE Conference and Expo Transportation Electrification Asia-Pacific (ITEC Asia-Pacific)*, 2014, pp. 1-6. doi: https://doi.org/10.1109/ITEC-AP.2014.6941033.
33. Stevanovic I., Wunsch B., Skibin S. Behavioral high-frequency modeling of electrical motors. *2013 Twenty-Eighth Annual IEEE Applied Power Electronics Conference and Exposition (APEC)*, 2013, pp. 2547-2550. doi: https://doi.org/10.1109/APEC.2013.6520654.
34. Thomas R.E., Rosa A.J., Toussaint G.J. *The Analysis and Design of Linear Circuits*. John Wiley & Sons, 2011. 928 p.
35. Nise N.S. *Control Systems Engineering*. Wiley Publ., 2015. 944 p.
36. Miloudi H., Bendaoud A., Miloudi M., Dickmann S., Schenke S. A novel method of transfer-function identification for modeling DM impedance of AC motor. *2017 International Symposium on Electromagnetic Compatibility - EMC EUROPE*, 2017, pp. 1-5. doi: https://doi.org/10.1109/EMCEurope.2017.8094770.
37. Antonini G. Spice equivalent circuits of frequency-domain responses. *IEEE Transactions on Electromagnetic Compatibility*, 2003, vol. 45, no. 3, pp. 502-512. doi: https://doi.org/10.1109/TEMC.2003.815528.

Yassine Hakmi[1], *PhD,*
Houcine Miloudi[1], *Professor,*
Mohamed Miloudi[2], *Lecturer,*
Abdelkader Gourbi[3], *Lecturer,*
Mohammed Hamza Bermaki[1], *Lecturer,*
[1] Djillali Liabes University, Algeria,
e-mail: yassine.hakmi@univ-sba.dz (Corresponding Author);
el.houcine@yahoo.fr; bermaki.hamza@gmail.com
[2] Relizane University, Algeria,
e-mail: mohamed.miloudi@univ-relizane.dz
[3] Ahmed Ben Bella University, Algeria,
e-mail: aekett@yahoo.fr